

Graphene nanoelectromechanical systems as valleytronic devices

Walter Ortiz ^{1,2,*}, Nikodem Szpak ^{3,†} and Thomas Stegmann ^{2,‡}

¹*Instituto de Investigación en Ciencias Básicas y Aplicadas, Universidad Autónoma del Estado de Morelos, 62209 Cuernavaca, Mexico*

²*Instituto de Ciencias Físicas, Universidad Nacional Autónoma de México, 62210 Cuernavaca, Mexico*

³*Fakultät für Physik, Universität Duisburg-Essen, 47057 Duisburg, Germany*



(Received 4 February 2022; revised 31 May 2022; accepted 30 June 2022; published 21 July 2022)

We investigate electronic transport in graphene nanoelectromechanical systems, known also as graphene nanodrums or nanomembranes. We demonstrate that these devices, despite their small values of strain between 0.1% and 1%, can be used as efficient and robust valley polarizers and filters. Their working principle is based on the pseudomagnetic field generated by the strain of the graphene membrane. They work for ballistic electron beams as well as for strongly dispersed ones and can be also used as electron beam collimators due to the focusing effect of the pseudomagnetic field. We show additionally that the current flow can be estimated by semiclassical trajectories which represent a computationally efficient tool for predicting the functionality of the devices.

DOI: [10.1103/PhysRevB.106.035416](https://doi.org/10.1103/PhysRevB.106.035416)

I. INTRODUCTION

Graphene, the wonder material of the 21st century, not only features pseudorelativistic electrons with conical dispersion relation but also facilitates two valleys located at the \mathbf{K}^+ and \mathbf{K}^- points of the Brillouin zone. This degree of freedom, interpreted as the valley spin of the electrons, suggests a new kind of electronics, named valleytronics [1], in which the valley spin is processed instead of the charge or the real spin. In recent years, several proposals have been made to create, manipulate, and detect valley-polarized currents in graphene [2–11], and even the idea of valley transistors has been put forward [12]. Although some impressive experimental progress has been made recently [13–17], valleytronics is still in its infancy because it remains challenging to control the valley-polarized currents [18].

In this paper, we show that graphene nanoelectromechanical systems (GrNEMS) [19–22] can be used to construct efficient and robust valley polarizers. We consider a graphene membrane that spans a cavity, as shown in Fig. 1. The membrane can be deformed in the unsupported region by an external stimulus, for example, the electric field of metallic gates [23–31]; by pressurized air [32,33]; or by periodic driving at the membrane eigenfrequencies [29,34] and forms a nanoelectromechanical system. Mechanical driving leads to membrane oscillations which, due to the ultrahigh electron mobility in graphene, can be treated as adiabatic changes in the background geometry in which the electronic current adjusts immediately to the quasistatic deformations [35–37]. Optical driving of the graphene membrane is also possible, but this leads in general to very small deformations [38].

The membranes can be sealed (or clamped) [26,39,40] and therefore are also called graphene nanodrums [29,30]. The deformation of the graphene membrane generates strain in the material. Its gradient induces a strong pseudomagnetic field which acts with opposite signs on the electrons in the two valleys [41–43] and thus can be used to spatially separate valley-polarized currents.

The appearance of strong pseudomagnetic fields in deformed graphene was previously utilized to propose valley filters [2–10], but to the best of our knowledge these devices have not yet been realized experimentally. One of the main obstacles is the challenge to fabricate properly deformed or strained graphene sheets, despite certain recent progress [44]. We demonstrate that graphene nanoresonators with already low strain values of the order of 0.1%–1% can be used to construct efficient valley polarizers. Even lower strain values can be used due to the possibility to place various resonators in

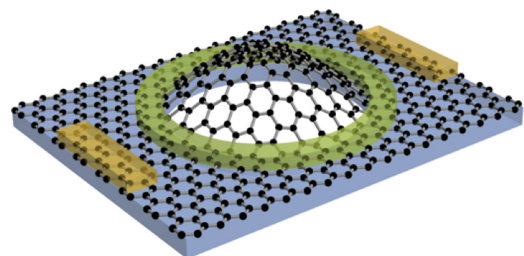


FIG. 1. Sketch of the investigated device. A graphene membrane is deposited on an insulating substrate with a circular cavity (blue shaded region). The graphene membrane is clamped at the edges using, for example, photoresist (green shaded ring), forming a nanodrum. The graphene membrane is deformed by the pressure of an external gas or the electric field of metallic gates (not shown). Current is injected and detected at the edges of the system (golden bars).

*balter20@gmail.com

†nikodem.szpak@uni-due.de

‡stegmann@icf.unam.mx

series [45–47]. Moreover, we show that the proposed devices can be applied to collimate and direct electrons and thus control the electronic transport.

II. MODEL OF THE GRAPHENE MEMBRANE

We consider graphene membranes with a size of about $300 \text{ nm} \times 600 \text{ nm}$, which are deposited on an insulating substrate with a cavity (see Fig. 1). We assume that the membrane is clamped at the edges of the cavity, for example, by means of photoresist [26,39,40]. The graphene membrane is modeled by the typical first nearest neighbor tight-binding Hamiltonian

$$H = -t_0 \sum_{i,j} |i^A\rangle \langle j^B| + \text{H.c.} \quad (1)$$

$|i^{A/B}\rangle$ indicate the atomic states localized on the carbon atoms at positions \mathbf{r}_i in sublattices A and B, respectively. The sum runs over nearest neighbor atoms, which are separated by a distance of $d_0 = 0.142 \text{ nm}$ and coupled with energy $t_0 = 2.8 \text{ eV}$. The minor effects of the substrate on the graphene membrane are neglected.

First, we consider circular cavities of radius r_0 where the deformation of the graphene membrane is given by the circular drum modes,

$$h_{mn}(r, \phi) = \begin{cases} a J_m(\lambda_{mn} r / r_0) \cos(m\phi) & \text{if } r \leq r_0, \\ 0 & \text{otherwise,} \end{cases} \quad (2)$$

where J_m is the m th Bessel function of the first kind and λ_{mn} is the n th zero of J_m . The amplitude of the deformation is controlled by the parameter a . Second, we consider also rectangular-shaped cavities of size $\mathcal{L} = L_x \times L_y$ with the deformation given by the rectangular drum modes,

$$h_{mn}(x, y) = \begin{cases} a \sin(n x / L_x) \sin(m y / L_y) & \text{if } x, y \in \mathcal{L}, \\ 0 & \text{otherwise.} \end{cases} \quad (3)$$

The deformations enlarge the distance of neighboring carbon atoms and weaken their coupling. This modification is, to good approximation, described by

$$t_{ij} \cong t_0 \exp(-\beta \delta_{ij}), \quad (4)$$

where $\delta_{ij} = \frac{|\mathbf{r}_i - \mathbf{r}_j| - d_0}{d_0}$ and $\beta = 3.37$ [6,48,49]. These deformations are motivated by the classical membrane modes and could be generated by mechanical periodic driving of the system at the corresponding eigenfrequencies [29,34] or by pressurized air [32,33].

In both cases, the real atomic structure of graphene can slightly deviate from our model, in which we assume a simple lift of atoms according to $z = h(x, y)$, creating strong strain at the boundary where the slope of h is the largest. A structural relaxation process using molecular dynamics may be applied to the deformed membrane in order to get closer to the experimental situation. We plan to address this point in future work.

III. ELECTRONIC TRANSPORT IN GRAPHENE

A. The Green's function method

The current flow in GrNEMS is studied by means of the Green's function method. Here we summarize the essential

equations of this method, as detailed introductions can be found in various textbooks [50,51].

The Green's function of the system is given by

$$G(E) = (E - H - \Sigma)^{-1}, \quad (5)$$

where E is the energy of the injected electrons and H is the tight-binding Hamiltonian (1). The self-energy $\Sigma = -i \sum_{i \in \text{edges}} |i\rangle \langle i|$ is a complex potential at the edges of the system which absorbs the electrons and suppresses finite-size effects.

Electrons are injected and detected through contacts at the edges of the system; see the golden bars in Fig. 1. We use two different models for the injection of the electrons. In the first one, the electrons are injected as plane waves represented by the inscattering function

$$\Sigma_{\text{pw}}^{\text{in}} = \sum_{i,j \in \text{contact}} A(\mathbf{r}_i) A(\mathbf{r}_j) \psi_j^*(\mathbf{k}) \psi_i(\mathbf{k}) |i\rangle \langle j|, \quad (6)$$

where the sum runs over the carbon atoms at the contact (see Fig. 1). $\psi_i(\mathbf{k})$ are the plane-wave eigenstates of graphene's Dirac Hamiltonian [see (14) below],

$$\psi_i(\mathbf{k}) = \begin{cases} c^- e^{i(\mathbf{k} + \mathbf{K}^-) \cdot \mathbf{r}_i} + c^+ e^{i(\mathbf{k} + \mathbf{K}^+) \cdot \mathbf{r}_i} & i \in A, \\ s c^- e^{i(\mathbf{k} + \mathbf{K}^-) \cdot \mathbf{r}_i + i\phi} - s c^+ e^{i(\mathbf{k} + \mathbf{K}^+) \cdot \mathbf{r}_i - i\phi} & i \in B, \end{cases} \quad (7)$$

where $\phi = \arg(ik_x + k_y)$. The parameters c^\pm control the occupation of the two \mathbf{K}^\pm valleys. In the following, we consider that for the injected electrons both valleys are fully mixed, i.e., $c_\pm = \pm 1/2$. The function

$$A(\mathbf{r}) = e^{-(\mathbf{k} \cdot (\mathbf{r} - \mathbf{r}_0) / w_0)^2} \quad (8)$$

gives the injected current beam a Gaussian profile. The parameters \mathbf{r}_0 and w_0 control the position and width of the beam. The advantage of this model is that it allows us to inject narrow electron beams with given energy, momentum, and valley polarization. Such beams are ideal to compare the current flow with semiclassical trajectories and phenomena from optics [4,42,52–54].

In the second case, we will use the so-called wideband model,

$$\Sigma_{\text{wb}}^{\text{in}} = \sum_{i,j \in \text{contact}} -i \eta |i\rangle \langle j|, \quad (9)$$

where the injecting contact is characterized by a constant, energy-independent surface density of states, $\text{DOS} \propto \eta = \text{const}$. In the following we set $\eta = t_0$, although our results do not depend crucially on that choice. Through this contact unpolarized electrons of energy E are injected without a precisely specified momentum, leading to a strongly divergent electron beam. This generic model represents well experimental situations where it is not precisely known how the electrons are entering the nanosystem via the contacts.

Finally, the current flowing between the atoms at positions \mathbf{r}_i and \mathbf{r}_j is calculated by

$$I_{ij} = \text{Im}[t_{ij} (G \Sigma^{\text{in}} G^\dagger)_{ij}]. \quad (10)$$

This bond current is then averaged (or coarse grained) over the six edges of the carbon hexagons.

B. Valley polarization

The valley polarization of a state $|\phi\rangle$ characterizes to what degree this state occupies the two valleys \mathbf{K}^\pm in graphene. It can be calculated by the projection $\mathcal{P}(\mathbf{k}) = |\langle\psi(\mathbf{k})|\phi\rangle|^2$ onto the graphene eigenfunctions (7). Within the Green's function approach this projection reads [3,4]

$$P_i(\mathbf{k}) = \langle\psi(\mathbf{k})|G\Sigma^{\text{in}}G^\dagger|\psi(\mathbf{k})\rangle_{A_i}. \quad (11)$$

It is calculated over a finite region A_i of the system (see, for example, the gray shaded regions in Fig. 4 below) in order to assess the valley polarization locally. The spectral density $P_i(\mathbf{k})$ is integrated around the valleys

$$\mathcal{P}_i^\pm = \int_{\mathbf{k}\in\mathbf{K}^\pm} d^2k P_i(\mathbf{k}), \quad (12)$$

and the valley polarization is given by

$$\mathcal{P}_i = \frac{\mathcal{P}_i^+ - \mathcal{P}_i^-}{\mathcal{P}_i^+ + \mathcal{P}_i^-}. \quad (13)$$

For $\mathcal{P}_i = \pm 1$ the electrons are localized exclusively at the \mathbf{K}^\pm valleys and hence are completely valley polarized, whereas for $\mathcal{P}_i = 0$ they are completely unpolarized.

IV. CONTINUOUS MODEL OF THE GRAPHENE MEMBRANE

A. Dirac equation for deformed graphene

At low energies, where the electron wavelength is larger than the lattice constant, the discrete tight-binding Hamiltonian (1) can be approximated by the continuous Dirac Hamiltonian [42,55–57]

$$H^D = i\hbar v_F \sigma^a e_a^l(\mathbf{x}) [\partial_l - iK_l^\pm(\mathbf{x})] \quad (14)$$

describing relativistic massless fermions. Here $v_F = 3t_0d_0/2\hbar$ is the Fermi velocity of the electrons, and σ^a ($a = 1, 2$) are the Pauli matrices. The local frame vectors

$$\mathbf{e}_a(\mathbf{x}) = [1 - \beta\hat{\varepsilon}(\mathbf{x})]\mathbf{e}_a \quad (15)$$

describe the curvature of the membrane and are determined by the strain tensor

$$\varepsilon_{ij} = \frac{1}{2} \partial_i h(\mathbf{x}) \partial_j h(\mathbf{x}) \quad (16)$$

multiplied by the factor $\beta > 1$. Hence, the effective deformation for the electrons is magnified by β but is otherwise identical to the real geometry of the deformed graphene membrane.

Due to the deformation, the two valleys, located in pristine graphene at $\mathbf{K}^\pm = (0, \pm\frac{4\pi}{3\sqrt{3}d_0})$, become a function of the position inside the device [41,58],

$$\mathbf{K}^\pm(\mathbf{x}) = \mathbf{K}^\pm \pm \frac{\beta}{2} (-2\varepsilon_{xy}, \varepsilon_{yy} - \varepsilon_{xx}). \quad (17)$$

This function can be interpreted formally as a vector potential, and its curl causes an effective pseudomagnetic field

$$\mathbf{B}^\pm(\mathbf{x}) = \pm \frac{\beta}{2} [\partial_x \varepsilon_{yy}(\mathbf{x}) - \partial_x \varepsilon_{xx}(\mathbf{x}) + 2\partial_y \varepsilon_{xy}(\mathbf{x})], \quad (18)$$

which is perpendicular to the graphene plane. In contrast to a true magnetic field, the pseudomagnetic field acts with

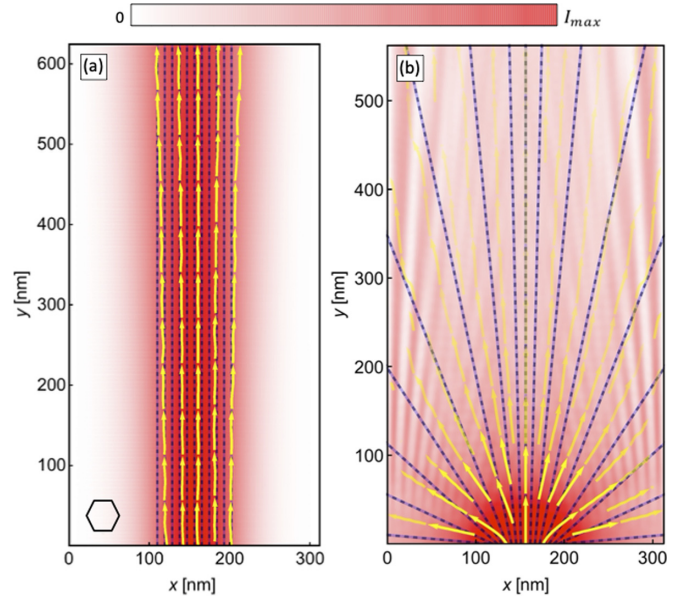


FIG. 2. Current flow in a pristine graphene membrane. The electrons are injected at the bottom armchair edge. The orientation of the graphene lattice is indicated by the small hexagon in the bottom left. The current vector field is given by the yellow arrows; its norm is given by the red shading. Solid blue lines and dashed black lines are semiclassical trajectories for electrons in valleys \mathbf{K}^+ and \mathbf{K}^- , respectively. (a) Ballistic beamlike current propagation is observed for electrons injected by the plane-wave model at energy $E = 200$ meV. (b) In the case of the generic wideband model the electrons, injected at a slightly lower energy of $E = 170$ meV, are dispersed strongly.

opposite signs in the two different valleys, preserving the time-reversal symmetry of the system. This sign change of the pseudomagnetic field will be used to separate spatially the electrons from different valleys.

B. Current flow lines in the geometric optics approximation

For smooth deformations on a scale larger than the electron wavelength the geometric optics approximations can be applied to the Hamiltonian (14). In our previous work [42], we showed that in this case the current flow can be predicted by the semiclassical trajectories of relativistic massless fermions,

$$\frac{dv^i}{d\tau} = -\Gamma_{kl}^i v^k v^l + \sqrt{g} g^{ij} \epsilon_{jk} v^k B^\pm, \quad (19)$$

where $v^i(\tau) = dx^i(\tau)/d\tau$ is the “velocity.” The first term on the right-hand side takes into account the curvature through the Christoffel symbols

$$\Gamma_{kl}^i = \frac{1}{2} g^{ij} (\partial_k g_{jl} + \partial_l g_{kj} - \partial_j g_{kl}). \quad (20)$$

The second term describes the electromagnetic force, where $g^{ij} = \delta_{ij} - 2\beta\varepsilon_{ij}(\mathbf{x})$ are the effective (inverse) metric and ϵ_{ij} is the Levi-Civita symbol in two dimensions. The calculation of these trajectories is computationally much less demanding than the quantitative quantum approach and independent of the system size. Therefore, it provides a useful tool to estimate the current flow in deformed graphene nanostructures.

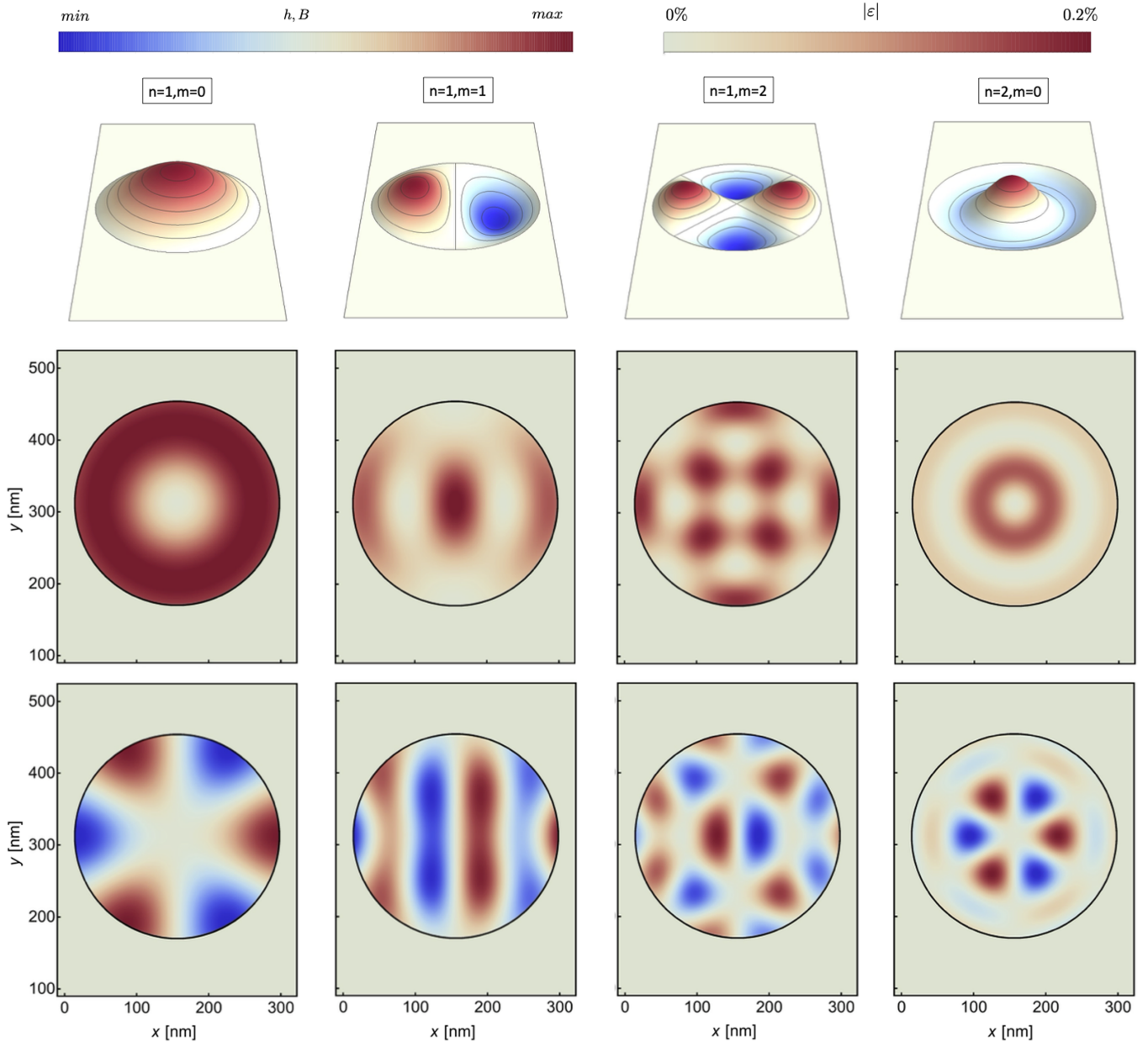


FIG. 3. Different modes (n, m) of a circular graphene nanodrum. The deformation profiles are shown in the top row. The resulting strain and pseudomagnetic fields can be found in the middle and bottom rows, respectively. The different drum modes lead to very distinct pseudomagnetic field patterns. The maximal values of the pseudomagnetic field amount to $B_{\max}^{\pm} \sim 1$ T.

V. RESULTS

We begin our discussion with Fig. 2, which shows the current flow in a pristine sheet of graphene. Electrons of energy $E = 200$ meV are injected at the bottom edge, which has the armchair shape. The current vector field is visualized by the yellow arrows, and its norm, the current density, is shown by the red shading.¹ On the left-hand side, the electrons are injected by means of the plane-wave model, resulting in

¹As the current shows some rare peaks, its maximum value is defined here as four standard deviations above the mean.

a ballistic beamlike propagation through the device. On the right-hand side, the generic wideband model is used for the injection of the current, which leads to a much more dispersed current flow. In this case, the electrons are partially reflected at the lateral edges (despite the absorbing contacts), leading to a ripple pattern in the current density due to interference. The current flow in graphene membranes will be described by one of the two models, depending on the experimental realization of the contacts.

We study here only static configurations since any graphene membrane dynamics (with oscillation frequencies ranging between 10 and 100 MHz for probes of size of $\sim 1 \mu\text{m}$ [59,60]) is so much slower than the timescale dictated by the

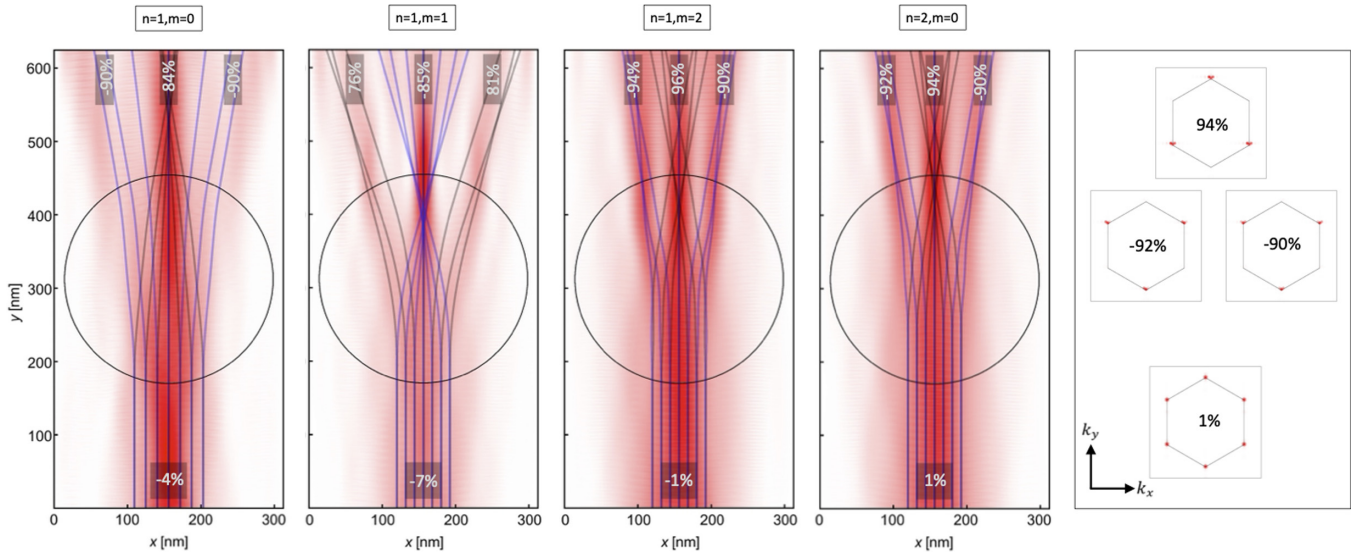


FIG. 4. Current flow in different drum modes (n, m) of circular graphene nanoresonators with a maximum strain ranging between 0.13% and 0.2%. The electrons, injected at $E = 200$ meV by the plane-wave model, are split into three beams. The black and blue solid lines are semiclassical trajectories for electrons in the K^+ and K^- valleys, respectively. These trajectories agree qualitatively with the current flow patterns and can be used to estimate the electronic transport in the device. The spectral densities P_i are calculated within the gray shaded rectangles and are shown for the (2,0) mode on the right. The resulting polarizations are given in percentages within the gray shaded rectangles and show that an initially unpolarized current is split into three valley-polarized beams.

electron mobility (~ 1 THz) that it can be treated as adiabatic change in the geometry to which the electronic current adjusts immediately [35–37].

A. Circular graphene nanodrums

We proceed with membranes deposited on a circular cavity with a diameter of 280 nm, forming a GrNEMS or graphene nanodrum. Figure 3 shows the deformation profile (top row), the strain (middle row), and the pseudomagnetic field (bottom row) for various drum modes (n, m). Figure 3 demonstrates that the shape of the pseudomagnetic field, which is perpendicular to the graphene sheet, changes drastically with the different drum modes.

The corresponding current flow pattern for electrons injected by the plane-wave model at energy $E = 200$ meV is shown in Fig. 4. It can be observed that the ballistic current is separated into three beams; two are deflected to the edges, while one goes through the center of the drum. The spectral density $P_i(\mathbf{k})$ of these current beams is calculated in the gray shaded rectangular regions and is shown in Fig. 4 (right) for the (2,0) mode. Close to the injecting source contact at the bottom edge, we observe small red dots in all six edges of graphene's Brillouin zone, which indicate that the electrons occupy both valleys and the current is unpolarized. In the regions at the upper edge, we observe red dots only at three equivalent Dirac points, proving that the current is fully valley polarized. Note that the dots in the central and in the outer regions are located in different valleys, and thus, the current in these regions is polarized in the opposite way. The spectral density, integrated around the different valleys, leads to the polarization \mathcal{P}_i , which is given in percentages in the rectangular regions of the current flow patterns. In general, we find that an initially unpolarized current is converted to a highly

valley polarized current $\mathcal{P}_i > 85\%$, which demonstrates clearly that the proposed device can be used as a valley polarizer or valley filter. The strain of the graphene membrane in the different drum modes lies in the range of 0.13% to 0.2%. This is an important feature of the proposed device because the experimentally achievable strain values are limited to a few percent or to values that are even lower, depending on the setup [32,33]. Note that close to the source contact small spurious valley polarizations of a few percent can appear due to the reflections of the electrons at the system edges, which are not completely suppressed by the complex damping potential.

The electron energy $E = 200$ meV corresponds to the Fermi wavelength $\lambda_F = 3\pi t_0 d_0 / E = 19$ nm, which is longer than the interatomic distances but shorter than typical length scales of the resonator modes. This makes it possible to estimate the current flow by means of semiclassical trajectories, which are given by the solution of the differential equation (19) and indicated in Fig. 4 by the solid blue and black curves for electrons from the K^+ and K^- valleys, respectively. These trajectories follow qualitatively the quantum current densities. Their behavior can be understood largely by taking into account the Lorenz force due to the pseudomagnetic field (see Fig. 3) acting on the electrons of different valleys with opposite signs. This Lorenz force focuses the electrons from one valley on a narrow beam that passes straight through the resonator, while the electrons from the other valley are deflected towards the edges. The trajectories also allow us to understand qualitatively the observed valley polarizations. Note that in the (1,1) mode the sign of the polarization is reversed compared to the other modes.

In the case of electron injection by the wideband model (see Fig. 5), the current flow is much more dispersed because in this model the electron energy is fixed ($E = 170$ meV)

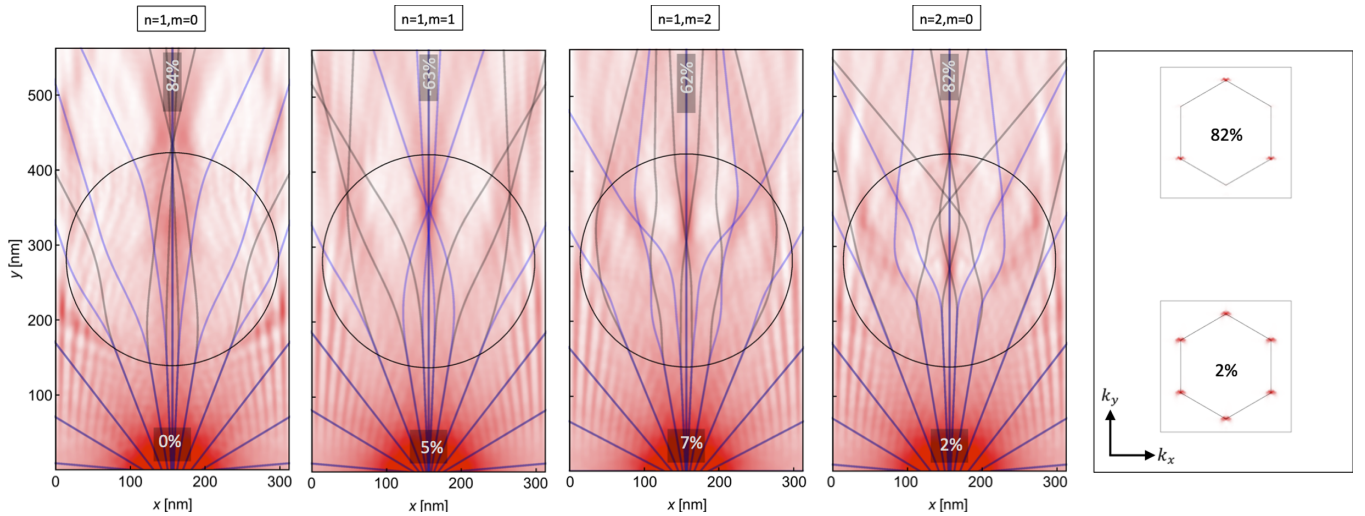


FIG. 5. Current flow for electrons injected at $E = 170$ meV by the wideband model. The maximal strain is in between 0.53% and 0.66%. The current is much more dispersed compared to the plane wave model, but part of the current is focused onto a narrow valley-polarized beam that passes through the center of the nanodrum. The current flow pattern agrees qualitatively with the semiclassical trajectories of strongly dispersive electrons. The spectral densities within the gray shaded regions of the (2,0) mode are shown on the right. The resulting polarizations are indicated in percentages.

but the momentum vector is unspecified. Nevertheless, we observe that part of the current density is deviated towards the edges, while another fraction of the current is focused on a beam that goes through the center of the resonator. The current flow can be understood qualitatively by the semiclassical trajectories if the initial spreading of the injected electron beam is taken into account. The valley polarization calculated at the bottom and top of the device confirms that valley polarization of up to 84% can be obtained, which is a surprisingly high value considering that the electrons are strongly dispersed and partially reflected at the system edges. The strain values used, which range between 0.53% and 0.66%, are slightly higher because stronger pseudomagnetic fields are required to focus the dispersive electron beam. The reason for slightly lowering the electron energy is to compensate the need for stronger pseudomagnetic fields and also to demonstrate the working principle for another parameter set.

We have selected the device parameters—resonator size, strain, and electron energy—to demonstrate its functionality at low pseudomagnetic fields ($B_{\max}^{\pm} \sim 1$ T) and low electron energies ($E \sim 200$ meV). These parameters not only permit numerical studies but can also be established experimentally. The device works not only for these specific parameters but within a rather ample parameter regime, as proven by means of Fig. 6, which shows an extended region of valley polarization $>80\%$. Moreover, from the structure of (19) it follows that the device properties remain unchanged when the size of the resonator and the amplitude a of the resonator modes [see (2) and (4)] are increased by the factor α , leaving the strain unchanged. As the amplitude is rather limited in experiments we can alternatively keep it constant, leading to a decrease in strain and pseudomagnetic field, which can then be compensated by decreasing the electron energy by the factor α^2 .

The device can be further improved by placing several nanoresonators in series, generating a valley-polarized and

collimated current beam (see Fig. 7). Note that in Fig. 7 the device is rotated by 90° but the current is still injected at the armchair edge. Such series of resonators could also be used to polarize electron beams of higher energy [61].

The time-dependent strain in the nanoresonators will generally also induce a pseudoelectric field $E^{\pm} = -\partial_t K^{\pm}$ [62,63]. Although the small strain values in the proposed device are capable of creating strong pseudomagnetic fields $B_{\max}^{\pm} \sim 1$ T, the pseudoelectric fields $E_{\max}^{\pm} \sim 40$ V/m, even for (an almost unrealistic) high resonance frequency of 1 GHz, lead to pseudovoltages of only a few microvolts across the device, which do not change the current flow and can be neglected.

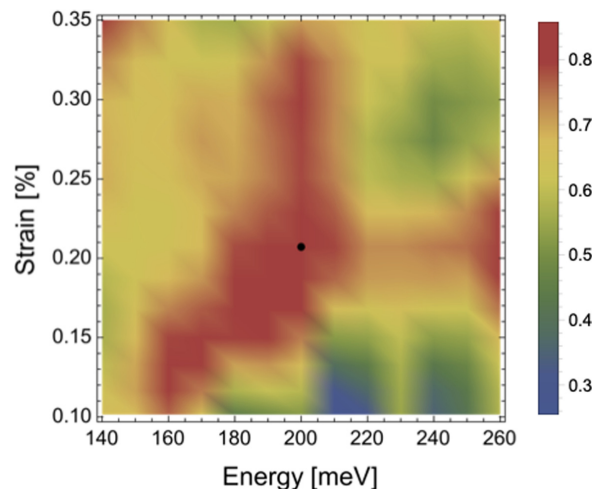


FIG. 6. Valley polarization as a function of the electron energy and strain for a circular graphene nanoresonator in the (1,0) mode. The valley polarization is calculated within the central region at the top edge. The small black dot indicates the parameters used in Fig. 4.

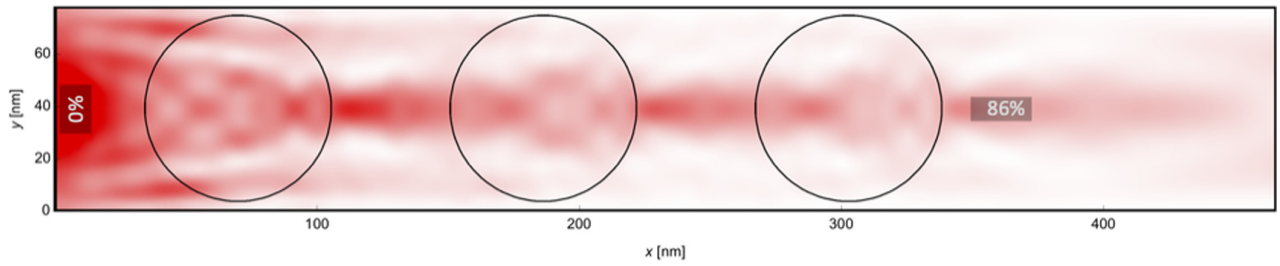


FIG. 7. Current flow in a device of three graphene nanodrums in series. The membrane is in the (1,0) mode with a maximum strain of 0.63%. The strongly dispersed electron beam, injected at the left edge, is strongly collimated by the resonator, demonstrating the rich functionality of nanodrum devices.

B. Rectangular graphene nanoresonators

We continue our study with rectangular graphene nanoresonators. The deformation, strain, and pseudomagnetic field patterns are shown in Fig. 8 for two different drum modes. Most notable is the fact that for an aspect ratio of $L_y/L_x = \sqrt{3}m/n$ the pseudomagnetic field is constant in the y

direction. This property, which can be proven easily by using Eqs. (4), (16), and (18), is rather stable and only lost slowly when the aspect ratio changes.

The current flow patterns for the plane-wave model of injection are shown in Fig. 9. In the case of the (1,1) mode, where a maximum strain of 1.5% is present, the electrons

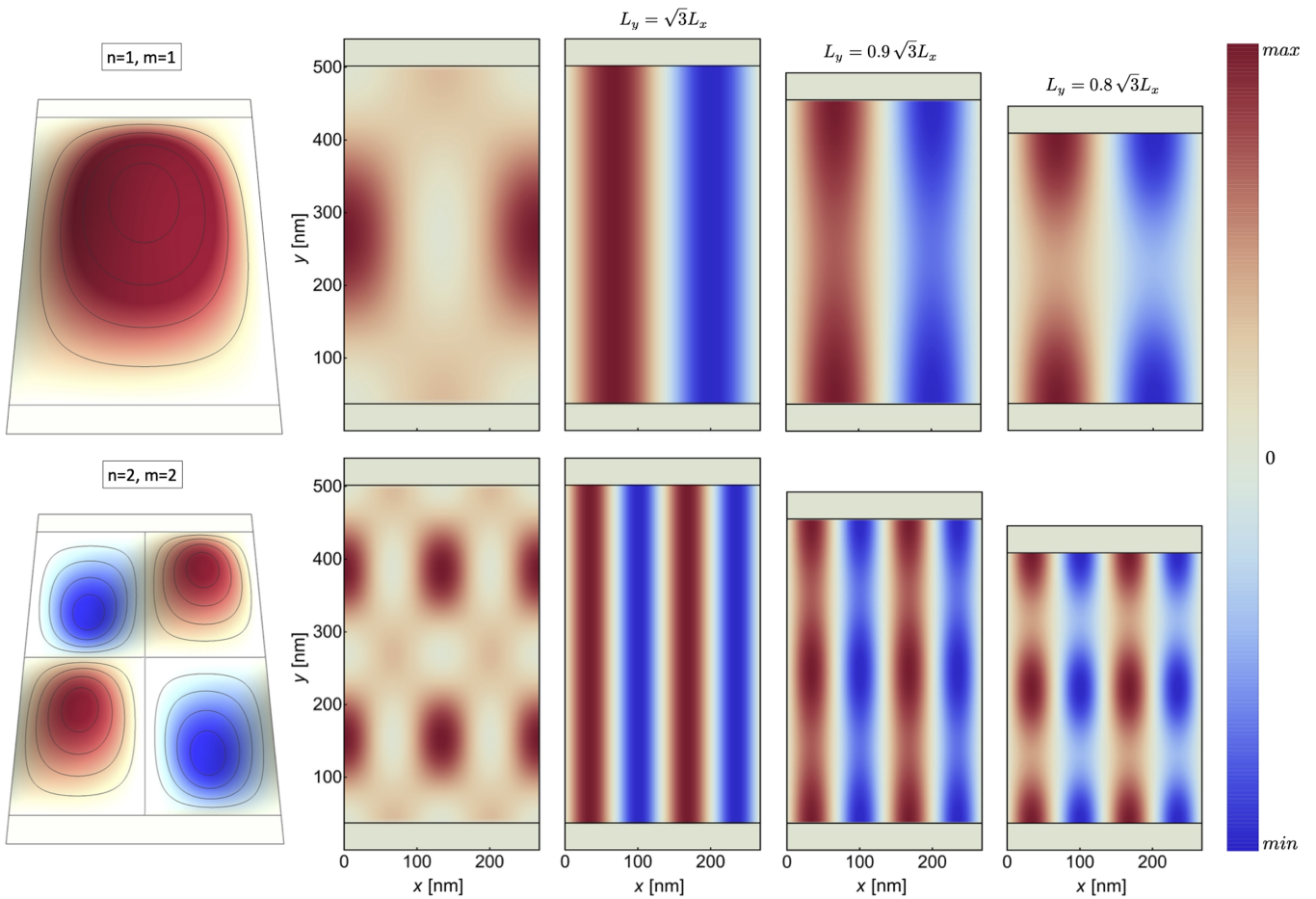


FIG. 8. Deformation profile (first column), strain (second column), and pseudomagnetic field (third column) of the $(n, m) = (1, 1)$ and $(2, 2)$ modes of a rectangular graphene nanoresonator. For an aspect ratio of $L_y/L_x = \sqrt{3}m/n$ the pseudomagnetic field is independent of the y coordinate and has a striplike shape. The alternating sign of the pseudomagnetic field in the strips is optimal to confine valley-polarized electron beams. The shape of the pseudomagnetic field is rather robust against variations of the aspect ratio; compare the third, fourth, and fifth columns.

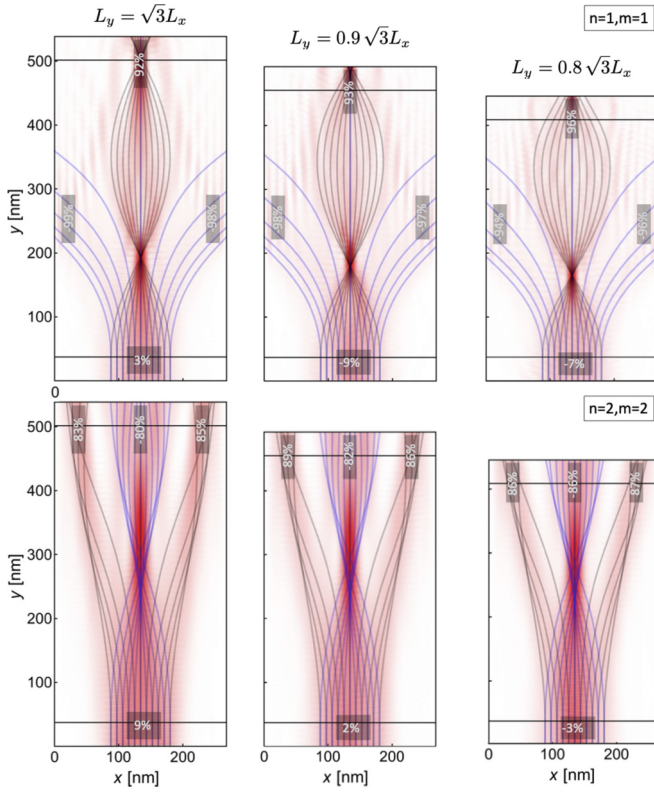


FIG. 9. Current flow in the $(n, m) = (1, 1)$ and $(2, 2)$ modes of a rectangular graphene nanoresonator. Electrons are injected at an energy of 200 meV by the plane-wave model. The edges of the resonator are indicated by black horizontal lines and the vertical system edges. The valley polarization is calculated and indicated within the gray shaded rectangular regions. The generation of narrow valley-polarized electron beams is observed, and they are stable if the aspect ratio is changed from its optimal value $L_y/L_x = \sqrt{3}m/n$. The semiclassical trajectories, indicated for the electrons in different valleys by the solid blue and black curves, follow qualitatively the current density. In particular, their crossing points agree with the focusing points of high current density.

from one valley are focused on a narrow beam in the center, while the electrons from the other valley are deviated towards the edges of the system. Note that these electrons are partially reflected at the edges, indicating that the absorption of the complex potential is not perfect. In the case of the $(2, 2)$ mode a maximum strain of 0.24% is applied, and the electrons are split into three narrow beams. The semiclassical trajectories agree well with the current flow. Most notably, the crossing points of the trajectories agree with the focusing points of the current density. The valley polarizations, measured and indicated in the gray rectangular regions in Fig. 9, demonstrate that highly valley polarized electron beams are generated with polarizations above 80%. Moreover, the current flow patterns and valley polarizations persist when the aspect ratio is changed from its optimal value. The striplike pseudomagnetic fields favor the generation of narrow beams of valley-polarized electrons. In the case of the $(1, 1)$ mode electrons from one valley are sorted out towards the edges, while in the $(2, 2)$ mode three valley-polarized beams are obtained.

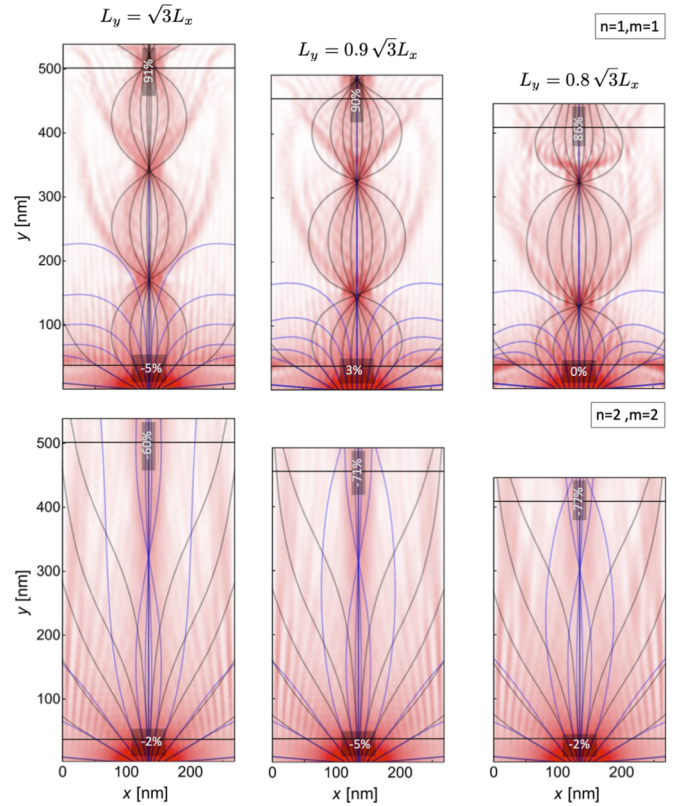


FIG. 10. Current flow for electrons injected by the wideband model at $E = 170$ meV. Part of the current density is confined in the central region of the device. Valley polarizations of about 90% in the $(1, 1)$ mode and 70% in the $(2, 2)$ mode are found. Due to the spreading of the electron beam stronger pseudomagnetic fields are necessary, and as a consequence, higher strain values of 4.4% and 0.35%, respectively, are needed. The semiclassical trajectories follow qualitatively the current density. Most impressively, their consecutive crossing points match the focusing points of the current density.

When we proceed with the wideband model of electron injection (see Fig. 10), the current becomes more dispersed (as in the case of circular nanodisks), but part of it is confined in a narrow region in the center of the device. This current shows valley polarizations of about 90% and 70% in the $(1, 1)$ and $(2, 2)$ modes, respectively. However, they go along with higher strain values of 4.4% and 0.35% for the two modes because stronger pseudomagnetic fields are necessary to focus the dispersed current flow and valley polarize the electrons. The semiclassical trajectories agree well with the current density. In particular, the consecutive crossing points of the trajectories match precisely the focusing points of the current density.

C. Current injection at the zigzag edge

In all devices presented in the previous sections the current has been injected at the armchair (bottom) edge. It might be tempting to inject the current also at the zigzag (left) edge and expect a clear separation of the valley-polarized beams. Due to the even number of stripes with nonvanishing pseudomagnetic

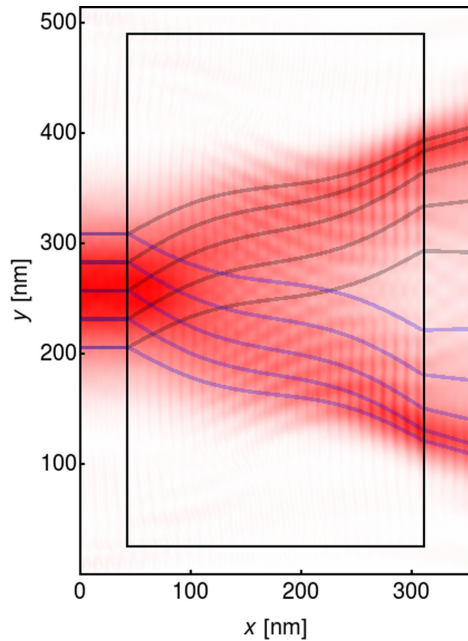


FIG. 11. Current flow for electrons injected at the left zigzag edge at $E = 200$ meV using the plane-wave model. The abrupt change in the strain at the left edge of the resonator (see Fig. 8) generates formally a singular pseudomagnetic field (along the black line) and leads to a sudden current splitting, for which the semiclassical trajectories must be specially adjusted.

field $B^\pm(\mathbf{x})$ the beams should finally become almost parallel; see the semiclassical trajectories in Fig. 11.

However, the situation at the zigzag boundary is very different from the armchair case. The pseudomagnetic vector potential $\mathbf{K}^\pm(\mathbf{x})$ is always parallel to the zigzag direction (i.e., has only a y component) and has a jump at the zigzag boundary which leads to formally infinite pseudomagnetic field $B^\pm(\mathbf{x})$. This forces the plane wave to abruptly change its propagation direction, depending on the valley polarization. At the same time, the strain tensor $\epsilon_{ij}(\mathbf{x})$ has a jump, too. Since these effects happen on a small scale, the continuous approximation can break down, and the current flow can differ significantly from the semiclassical trajectories. Nevertheless, after adjusting the trajectories to the kicklike velocity change, we find a quite good agreement between the quantum and semiclassical currents (see Fig. 11). The abrupt change in the strain is an artifact of our simple model of the graphene nanodrum. In order to obtain a more realistic picture one should consider smoother edges of the membrane. The above-mentioned relaxation of the atomic structure should modify

the strain distribution exactly in this direction. This point is the focus of our ongoing research and will be addressed elsewhere.

VI. CONCLUSIONS

We have demonstrated that GrNEMS can be used as efficient valley polarizers. In the case of circular graphene nanodrums strain values already between 0.1% and 0.6% lead to highly polarized currents. The device works for the plane-wave model, where the electrons are injected as a narrow ballistic beam, as well as for the wideband model, where the injected current is strongly dispersive. In the latter case, higher strain values and thus stronger pseudomagnetic fields are able to not only valley polarize the electrons but also focus them to a narrow beam acting as a beam collimator.

In the case of rectangular nanoresonators, we found that a special aspect ratio of $L_y/L_x = \sqrt{3}m/n$ for the drum mode (m, n) leads to a stripelike pseudomagnetic field, constant along the y direction, which optimally confines the valley-polarized electrons beams. The semiclassical trajectories agree well with the current calculated by means of the Green's function method. Most impressively, their crossing points agree precisely with the focusing points of the current density. These trajectories represent a computationally efficient tool to predict the current flow in graphene nanostructures, especially in larger systems in which a direct lattice simulation is no more possible. These trajectories allowed us to predict the device functionality even in larger resonators.

For the experimental realization of the proposed device, high-quality samples of graphene will be favorable. Lattice imperfections, finite temperature, and even the substrate will reduce the mean free path and the mobility of the electrons, but our device should be rather robust against these perturbations because the pseudomagnetic field not only valley polarizes the electrons but also refocuses them (see Figs. 4 and 7). A possible obstacle to fabricate the device which also exists in other proposals based on the pseudomagnetic field is the fact that the pseudomagnetic field is not rotationally invariant and thus the orientation of the graphene lattice with respect to the contacts has to be controlled during fabrication.

ACKNOWLEDGMENTS

W.O. gratefully acknowledges a CONACYT graduate scholarship. W.O. and T.S. gratefully acknowledge funding from CONACYT Project No. A1-S-13469 and UNAM-PAPIIT Projects No. IA103020 and No. IN103922. N.S. gratefully acknowledges funding by the Deutsche Forschungsgemeinschaft (DFG, German Research Foundation), Project No. 278162697 – SFB 1242.

- [1] J. R. Schaibley, H. Yu, G. Clark, P. Rivera, J. S. Ross, K. L. Seyler, W. Yao, and X. Xu, Valleytronics in 2D materials, *Nat. Rev. Mater.* **1**, 16055 (2016).
 [2] J. Wang, Z. Lin, and K. S. Chan, Pure valley current generation in graphene with a Dirac gap by quantum pumping, *Appl. Phys. Express* **7**, 125102 (2014).

- [3] M. Settnes, S. R. Power, M. Brandbyge, and A.-P. Jauho, Graphene Nanobubbles as Valley Filters and Beam Splitters, *Phys. Rev. Lett.* **117**, 276801 (2016).
 [4] T. Stegmann and N. Szpak, Current splitting and valley polarization in elastically deformed graphene, *2D Mater.* **6**, 015024 (2019).

- [5] S. P. Milovanović and F. M. Peeters, Strain controlled valley filtering in multi-terminal graphene structures, *Appl. Phys. Lett.* **109**, 203108 (2016).
- [6] R. Carrillo-Bastos, C. León, D. Faria, A. Latgé, E. Y. Andrei, and N. Sandler, Strained fold-assisted transport in graphene systems, *Phys. Rev. B* **94**, 125422 (2016).
- [7] D. Zhai and N. Sandler, Local versus extended deformed graphene geometries for valley filtering, *Phys. Rev. B* **98**, 165437 (2018).
- [8] R. Carrillo-Bastos, M. Ochoa, S. A. Zavala, and F. Mireles, Enhanced asymmetric valley scattering by scalar fields in nonuniform out-of-plane deformations in graphene, *Phys. Rev. B* **98**, 165436 (2018).
- [9] M. T. Mahmud and N. Sandler, Emergence of strain-induced moiré patterns and pseudomagnetic field confined states in graphene, *Phys. Rev. B* **102**, 235410 (2020).
- [10] F. Solomon and S. R. Power, Valley current generation using biased bilayer graphene dots, *Phys. Rev. B* **103**, 235435 (2021).
- [11] M. S. Mrudul, Á. Jiménez-Galán, M. Ivanov, and G. Dixit, Light-induced valleytronics in pristine graphene, *Optica* **8**, 422 (2021).
- [12] M.-K. Lee, N.-Y. Lue, C.-K. Wen, and G. Y. Wu, Valley-based field-effect transistors in graphene, *Phys. Rev. B* **86**, 165411 (2012).
- [13] F. Guinea, M. I. Katsnelson, and A. K. Geim, Energy gaps and a zero-field quantum Hall effect in graphene by strain engineering, *Nat. Phys.* **6**, 30 (2010).
- [14] P. Nemes-Incze, G. Kukucska, J. Koltai, J. Kürti, C. Hwang, L. Tapasztó, and L. P. Biró, Preparing local strain patterns in graphene by atomic force microscope based indentation, *Sci. Rep.* **7**, 3035 (2017).
- [15] A. Georgi, P. Nemes-Incze, R. Carrillo-Bastos, D. Faria, S. V. Kusminskiy, D. Zhai, M. Schneider, D. Subramaniam, T. Mashoff, N. M. Freitag, M. Liebmann, M. Pratzler, L. Wirtz, C. R. Woods, R. V. Gorbachev, Y. Cao, K. S. Novoselov, N. Sandler, and M. Morgenstern, Tuning the pseudospin polarization of graphene by a pseudomagnetic field, *Nano Lett.* **17**, 2240 (2017).
- [16] P. Jia, W. Chen, J. Qiao, M. Zhang, X. Zheng, Z. Xue, R. Liang, C. Tian, L. He, Z. Di, and X. Wang, Programmable graphene nanobubbles with three-fold symmetric pseudo-magnetic fields, *Nat. Commun.* **10**, 3127 (2019).
- [17] P. Nigge, A. C. Qu, É. Lantagne-Hurtubise, E. Mårzell, S. Link, G. Tom, M. Zonno, M. Michiardi, M. Schneider, S. Zhdanovich, G. Levy, U. Starke, C. Gutiérrez, D. Bonn, S. A. Burke, M. Franz, and A. Damascelli, Room temperature strain-induced Landau levels in graphene on a wafer-scale platform, *Sci. Adv.* **5**, eaaw5593 (2019).
- [18] D. Faria, C. León, L. R. F. Lima, A. Latgé, and N. Sandler, Valley polarization braiding in strained graphene, *Phys. Rev. B* **101**, 081410(R) (2020).
- [19] C. Chen and J. Hone, Graphene nanoelectromechanical systems, *Proc. IEEE* **101**, 1766 (2013).
- [20] A. Castellanos-Gomez, V. Singh, H. S. J. van der Zant, and G. A. Steele, Mechanics of freely-suspended ultrathin layered materials, *Ann. Phys. (Berlin, Ger.)* **527**, 27 (2015).
- [21] Z. H. Khan, A. R. Kermany, A. Öchsner, and F. Iacopi, Mechanical and electromechanical properties of graphene and their potential application in MEMS, *J. Phys. D* **50**, 053003 (2017).
- [22] M. C. Lemme, S. Wagner, K. Lee, X. Fan, G. J. Verbiest, S. Wittmann, S. Lukas, R. J. Dolleman, F. Niklaus, H. S. J. van der Zant, G. S. Duesberg, and P. G. Steeneken, Nanoelectromechanical sensors based on suspended 2D materials, *Research (Washington, DC, U.S.)* **2020**, 8748602 (2020).
- [23] C. Chen, S. Rosenblatt, K. I. Bolotin, W. Kalb, P. Kim, I. Kymissis, H. L. Stormer, T. F. Heinz, and J. Hone, Performance of monolayer graphene nanomechanical resonators with electrical readout, *Nat. Nanotechnol.* **4**, 861 (2009).
- [24] C.-L. Wong, M. Annamalai, Z.-Q. Wang, and M. Palaniapan, Characterization of nanomechanical graphene drum structures, *J. Micromech. Microeng.* **20**, 115029 (2010).
- [25] Y. Xu, C. Chen, V. V. Deshpande, F. A. DiRenno, A. Gondarenko, D. B. Heinz, S. Liu, P. Kim, and J. Hone, Radio frequency electrical transduction of graphene mechanical resonators, *Appl. Phys. Lett.* **97**, 243111 (2010).
- [26] S. Lee, C. Chen, V. V. Deshpande, G.-H. Lee, I. Lee, M. Lekas, A. Gondarenko, Y.-J. Yu, K. Shepard, P. Kim, and J. Hone, Electrically integrated SU-8 clamped graphene drum resonators for strain engineering, *Appl. Phys. Lett.* **102**, 153101 (2013).
- [27] J. P. Mathew, R. N. Patel, A. Borah, R. Vijay, and M. M. Deshmukh, Dynamical strong coupling and parametric amplification of mechanical modes of graphene drums, *Nat. Nanotechnol.* **11**, 747 (2016).
- [28] R. D. Alba, F. Massel, I. R. Storch, T. S. Abhilash, A. Hui, P. L. McEuen, H. G. Craighead, and J. M. Parpia, Tunable phonon-cavity coupling in graphene membranes, *Nat. Nanotechnol.* **11**, 741 (2016).
- [29] D. Davidovikj, J. J. Slim, S. J. Cartamil-Bueno, H. S. J. van der Zant, P. G. Steeneken, and W. J. Venstra, Visualizing the motion of graphene nanodrums, *Nano Lett.* **16**, 2768 (2016).
- [30] D. Davidovikj, M. Poot, S. J. Cartamil-Bueno, H. S. J. van der Zant, and P. G. Steeneken, On-chip heaters for tension tuning of graphene nanodrums, *Nano Lett.* **18**, 2852 (2018).
- [31] J. Güttinger, A. Noury, P. Weber, A. M. Eriksson, C. Lagoin, J. Moser, C. Eichler, A. Wallraff, A. Isacsson, and A. Bachtold, Energy-dependent path of dissipation in nanomechanical resonators, *Nat. Nanotechnol.* **12**, 631 (2017).
- [32] Y. Shin, M. Lozada-Hidalgo, J. L. Sambricio, I. V. Grigorieva, A. K. Geim, and C. Casiraghi, Raman spectroscopy of highly pressurized graphene membranes, *Appl. Phys. Lett.* **108**, 221907 (2016).
- [33] A. D. Smith, F. Niklaus, A. Paussa, S. Schröder, A. C. Fischer, M. Sterner, S. Wagner, S. Vaziri, F. Forsberg, D. Esseni, M. Östling, and M. C. Lemme, Piezoresistive properties of suspended graphene membranes under uniaxial and biaxial strain in nanoelectromechanical pressure sensors, *ACS Nano* **10**, 9879 (2016).
- [34] J. Atalaya, A. Isacsson, and J. M. Kinaret, Continuum elastic modeling of graphene resonators, *Nano Lett.* **8**, 4196 (2008).
- [35] A. M. Eriksson, D. Midtvedt, A. Croy, and A. Isacsson, Frequency tuning, nonlinearities and mode coupling in circular mechanical graphene resonators, *Nanotechnology* **24**, 395702 (2013).
- [36] X. Zhang, R. Waitz, F. Yang, C. Lutz, P. Angelova, A. Götzhäuser, and E. Scheer, Vibrational modes of ultrathin carbon nanomembrane mechanical resonators, *Appl. Phys. Lett.* **106**, 063107 (2015).

- [37] B. S. Popescu and A. Croy, Efficient auxiliary-mode approach for time-dependent nanoelectronics, *New J. Phys.* **18**, 093044 (2016).
- [38] D. Miller and B. Alemán, Spatially resolved optical excitation of mechanical modes in graphene NEMS, *Appl. Phys. Lett.* **115**, 193102 (2019).
- [39] C. Chen, S. Lee, V. V. Deshpande, G.-H. Lee, M. Lekas, K. Shepard, and J. Hone, Graphene mechanical oscillators with tunable frequency, *Nat. Nanotechnol.* **8**, 923 (2013).
- [40] M. Lee, D. Davidovikj, B. Sajadi, M. Šiškins, F. Alijani, H. S. J. van der Zant, and P. G. Steeneken, Sealing graphene nanodrums, *Nano Lett.* **19**, 5313 (2019).
- [41] M. Vozmediano, M. Katsnelson, and F. Guinea, Gauge fields in graphene, *Phys. Rep.* **496**, 109 (2010).
- [42] T. Stegmann and N. Szpak, Current flow paths in deformed graphene: From quantum transport to classical trajectories in curved space, *New J. Phys.* **18**, 053016 (2016).
- [43] G. G. Naumis, S. Barraza-Lopez, M. Oliva-Leyva, and H. Terrones, Electronic and optical properties of strained graphene and other strained 2D materials: A review, *Rep. Prog. Phys.* **80**, 096501 (2017).
- [44] Z. Dai, L. Liu, and Z. Zhang, Strain engineering of 2D materials: Issues and opportunities at the interface, *Adv. Mater.* **31**, 1805417 (2019).
- [45] A. M. van der Zande, R. A. Barton, J. S. Alden, C. S. Ruiz-Vargas, W. S. Whitney, P. H. Q. Pham, J. Park, J. M. Parpia, H. G. Craighead, and P. L. McEuen, Large-scale arrays of single-layer graphene resonators, *Nano Lett.* **10**, 4869 (2010).
- [46] R. A. Barton, B. Ilic, A. M. van der Zande, W. S. Whitney, P. L. McEuen, J. M. Parpia, and H. G. Craighead, High, size-dependent quality factor in an array of graphene mechanical resonators, *Nano Lett.* **11**, 1232 (2011).
- [47] X. Liu, J. W. Suk, N. G. Boddeti, L. Cantley, L. Wang, J. M. Gray, H. J. Hall, V. M. Bright, C. T. Rogers, M. L. Dunn, R. S. Ruoff, and J. S. Bunch, Large arrays and properties of 3-terminal graphene nanoelectromechanical switches, *Adv. Mater.* **26**, 1571 (2014).
- [48] V. M. Pereira, A. H. Castro Neto, and N. M. R. Peres, Tight-binding approach to uniaxial strain in graphene, *Phys. Rev. B* **80**, 045401 (2009).
- [49] R. M. Ribeiro, V. M. Pereira, N. M. R. Peres, P. R. Briddon, and A. H. C. Neto, Strained graphene: Tight-binding and density functional calculations, *New J. Phys.* **11**, 115002 (2009).
- [50] S. Datta, *Electronic Transport in Mesoscopic Systems* (Cambridge University Press, Cambridge, 1997).
- [51] S. Datta, *Quantum Transport: Atom to Transistor* (Cambridge University Press, Cambridge, 2005).
- [52] Y. Betancur-Ocampo, F. Leyvraz, and T. Stegmann, Electron optics in phosphorene pn junctions: Negative reflection and anti-super-Klein tunneling, *Nano Lett.* **19**, 7760 (2019).
- [53] Y. Betancur-Ocampo, E. Paredes-Rocha, and T. Stegmann, Phosphorene pnp junctions as perfect electron waveguides, *J. Appl. Phys.* **128**, 114303 (2020).
- [54] E. Paredes-Rocha, Y. Betancur-Ocampo, N. Szpak, and T. Stegmann, Gradient-index electron optics in graphene *p-n* junctions, *Phys. Rev. B* **103**, 045404 (2021).
- [55] F. de Juan, M. Sturla, and M. A. H. Vozmediano, Space Dependent Fermi Velocity in Strained Graphene, *Phys. Rev. Lett.* **108**, 227205 (2012).
- [56] F. de Juan, J. L. Mañes, and M. A. H. Vozmediano, Gauge fields from strain in graphene, *Phys. Rev. B* **87**, 165131 (2013).
- [57] M. Oliva-Leyva and G. G. Naumis, Generalizing the Fermi velocity of strained graphene from uniform to nonuniform strain, *Phys. Lett. A* **379**, 2645 (2015).
- [58] A. H. Castro Neto, F. Guinea, N. M. R. Peres, K. S. Novoselov, and A. K. Geim, The electronic properties of graphene, *Rev. Mod. Phys.* **81**, 109 (2009).
- [59] D. R. Cooper, B. D'Anjou, N. Ghattamaneni, B. Harack, M. Hilke, A. Horth, N. Majlis, M. Massicotte, L. Vandsburger, E. Whiteway, and V. Yu, Experimental review of graphene, *Int. Scholarly Res. Not.* **2012**, 501686 (2012).
- [60] F.-T. Shi, S.-C. Fan, C. Li, and Z.-A. Li, Opto-thermally excited Fabry-Perot resonance frequency behaviors of clamped circular graphene membrane, *Nanomaterials* **9**, 563 (2019).
- [61] V. Torres, P. Silva, E. A. T. de Souza, L. A. Silva, and D. A. Bahamon, Valley notch filter in a graphene strain superlattice: Green's function and machine learning approach, *Phys. Rev. B* **100**, 205411 (2019).
- [62] F. von Oppen, F. Guinea, and E. Mariani, Synthetic electric fields and phonon damping in carbon nanotubes and graphene, *Phys. Rev. B* **80**, 075420 (2009).
- [63] E. Sela, Y. Bloch, F. von Oppen, and M. B. Shalom, Quantum Hall Response to Time-Dependent Strain Gradients in Graphene, *Phys. Rev. Lett.* **124**, 026602 (2020).